Shock equation of state of ^{6}LiH to 1.1 TPa

A. Lazicki,[1] R. A. London,[1] F. Coppari,[1] D. Erskine,[1] H. D. Whitley,[1] K. J. Caspersen,[1] D. E. Fratanduono,[1] M. A. Morales,[1] P. M. Celliers,[1] J. H. Eggert,[1] M. Millot,[1] D. C. Swift,[1] G. W. Collins,[2] S. O. Kucheyev,[1] J. I. Castor,[1] and J. Nilsen[1]

[1]*Lawrence Livermore National Laboratory, 7000 East Avenue, Livermore, California 94550, USA*

[2]*Department of Mechanical Engineering, University of Rochester, Rochester, New York 14623, USA*

(Received 1 November 2016; revised manuscript received 31 July 2017; published 2 October 2017)

Using laser-generated shock waves, we have measured pressure, density, and temperature of LiH on the principal Hugoniot between 260 and 1100 GPa (2.6–11 Mbar) and on a second-shock Hugoniot up to 1400 GPa to near fivefold compression, extending the maximum pressure reached in non-nuclear experiments by a factor of two. We observe the onset of metal-like reflectivity consistent with temperature-induced ionization of the Li 2s electron, and no sign of additional changes in ionization up to the maximum pressure. Our measurements are in good agreement with gas gun, Z-machine, and underground test data and are accurately described by quantum molecular dynamics simulations. The results confirm the validity of equation of state models built on an average-atom description of the electron-thermal contribution to the free energy and a density-dependent Grüneisen parameter to describe shock response of LiH over this pressure range.

DOI: 10.1103/PhysRevB.96.134101

I. INTRODUCTION

Lithium hydride has received a lot of attention in the literature because of its potential for use in nuclear reactors [1] and as a hydrogen storage material [2]. An accurate description of the properties of this compound also serves as a benchmark for theoretical models due to its simple electronic structure and the influence of zero-point motion on its high-pressure equation of state (EOS) [3]. For example, the conditions for an expected structural and electronic transformation in the solid phase differ widely depending on the electron correlation model chosen for various density functional theory (DFT) simulations [4]. Models for the equation of state in the plasma phase also differ depending on their treatment of the electron, ion, and thermal contributions to the free energy, and there are very few experiments constraining these models above a few hundred gigapascals. As a result, recent work on EOS models for various materials have utilized a variety of *ab initio* simulation methods [5–8]. LiH is particularly challenging for high-temperature EOS modeling due to its relatively low ratio of electrons to ions. For higher-Z materials, the electron-thermal free energy term typically represents the largest contribution to the EOS in the plasma and warm dense phases due to the large number of electrons compared to ions. In lower-Z materials, the ionic contribution to the EOS is of higher relative significance. Recent studies of carbon [5], for example, have revealed that typical models [9] for the ion thermal contribution to the EOS fail to model free energies computed via quantum molecular dynamics simulations. This study was performed to extend the range of LiH experimental data into the TPa pressure regime, both to inform *ab initio* calculations and to directly refine the EOS free-energy models.

II. METHODS

The experimental setup is shown in Fig. 1. All experiments were performed at the Omega laser facility at the Laboratory for Laser Energetics in Rochester, NY. ^{6}LiH material was acquired from the Y12 National Security Complex, and all samples used in this study were freshly cleaved from the same large single crystal. We used two different target designs. For the majority of the shots, LiH crystals were sandwiched between windows of quartz [Fig. 1(a)], which served as an impedance-matching standard. LiH is hygroscopic so all samples were prepared under high-purity argon gas in an inert atmosphere glovebox (<1 ppm O_2). To protect the LiH crystals from reaction after removal from the glovebox, all targets were encapsulated around the perimeter with a continuous layer of epoxy. LiH also reacts chemically with the dangling hydroxyl groups present in epoxy, so the ^{6}LiH sample was surrounded with a thin layer of dry mineral oil. As a result, there were micron-scale layers of mineral oil at the interfaces between the LiH sample and the quartz windows. The ablator consisted of 10–30 μm of CH plastic. A 2–5 μm deposited layer of gold between the ablator and quartz standard absorbed x rays created during CH ablation, preventing LiH preheating.

For the second target type [Fig. 1(b)], sample exposure to atmosphere was avoided (and gaps at interfaces eliminated) by compressing a layer of single crystal LiH to a few kbar between a 200- or 350-μm flat diamond anvil and a 5-mm sapphire anvil in a Merrill-Bassett–type anvil cell [10]. The thickness of the diamond anvil (necessary in order to exert pressure without cracking) limited the LiH shock pressure since the shock wave decayed as it passed through the diamond before entering the LiH. A stainless steel gasket with a 1-mm-diameter hole contained the sample laterally. Upon compression, the hole shrank to 0.6 mm. A $300 \times 300 \times 30$-μm square of quartz affixed to the diamond anvil with a micron-scale layer of vacuum grease and in contact with the LiH sample served as the equation-of-state standard. A 2-μm Au preheat shield and a 15-μm CH ablator were deposited on the outside of the diamond anvil. The initial pressure (<1 GPa) in the sample chamber prior the shot was determined from the pressure-induced energy shift of fluorescence from micron-scale ruby crystals placed near the quartz crystal [11]. The effect of the exerted pressure on the initial density of the quartz and LiH crystals was determined from the pressure-density equations of state from Refs. [12,13]. The increase in initial LiH density as a result of precompression was less than 3% for all shots.

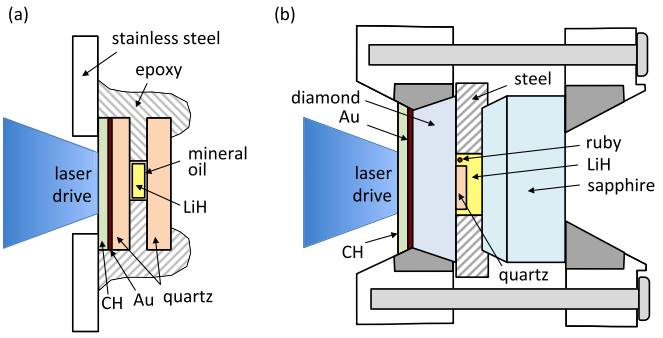

FIG. 1. Experimental configurations: (a) single-crystal ^{6}LiH encapsulated in dry mineral oil and sealed with epoxy between quartz windows and (b) single-crystal ^{6}LiH compressed to a few kbar between diamond and sapphire anvils in a pressure cell, together with a quartz standard and ruby pressure calibrant. Both configurations use an Au preheat shield and CH ablator.

The target was driven with up to 12 beams of the Omega laser, with top-hat pulse shapes 1–1.6 ns in length, energies of 400–500 J/beam and a spot size of 800 μm at full-width half maximum, formed using distributed phase plates. The intensity on target ranged from 5×10^{13} to 5×10^{14} W/cm^2. Shock velocities in the quartz reference windows and in LiH were tracked using a velocity interferometer system for any reflector (VISAR) diagnostic [14,15]. The velocity sensitivities of the interferometers were chosen to minimize measurement uncertainty over the range of drive pressures and varied between 2.73 and 16.1 km/s/fringe. Thermal emission was detected using a streaked optical pyrometer (SOP) diagnostic [16]. In a subset of the shots, the shock transmitted from the LiH into the second quartz window was also recorded, yielding data corresponding to a reshock from the higher-impedance

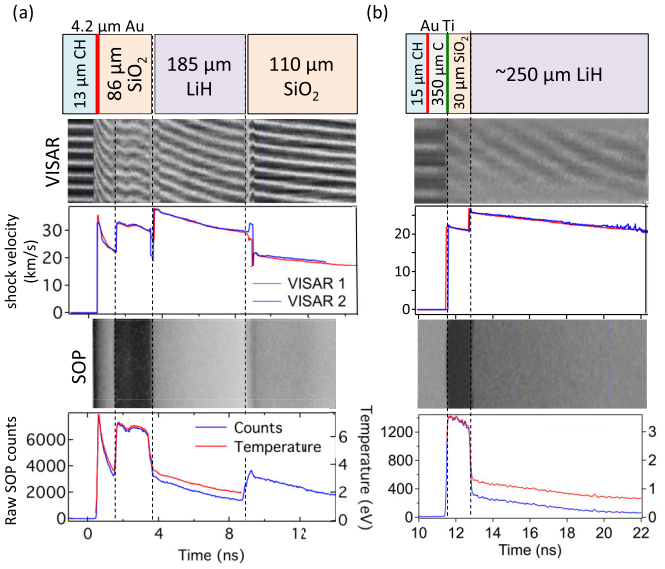

FIG. 2. Sample VISAR data with analyzed shock velocity and SOP data with analyzed temperature in (a) the first target type in which LiH was encased in mineral oil and sandwiched between quartz plates (shot 72663) and (b) the second target type in which LiH was contained in a piston-cylinder pressure cell (shot 66034).

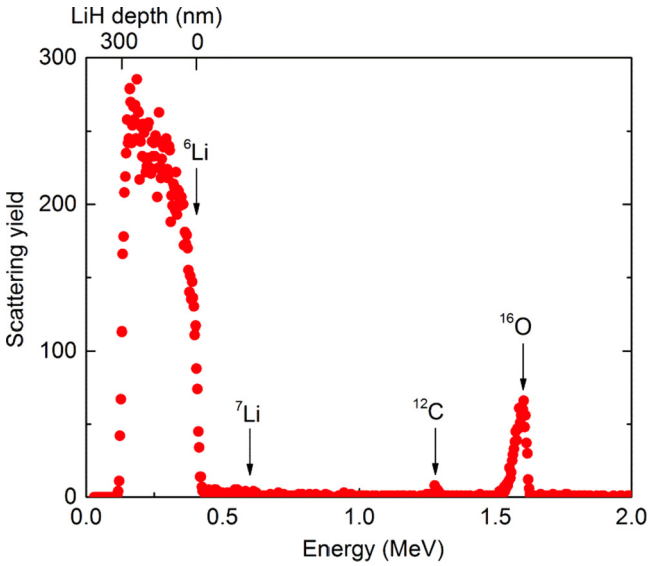

FIG. 3. Rutherford backscattering spectrum from a representative LiH sample, revealing that the sample contains ^{6}Li with trace C and O surface contamination of $\sim 10^{16}$ and $\sim 10^{17}$ at/cm^2, respectively. The ^{7}Li/^{6}Li atomic fraction is below 5 at.%. Surface peaks of the elements detected are indicated by arrows.

quartz back into the lower-impedance LiH. Examples of the raw data and the velocity and temperature analysis for the two target types are shown in Fig. 2.

III. LIH CHARACTERIZATION

LiH is sufficiently lightweight that the Li and H isotopics have a marked effect on the initial density. The elemental composition of LiH crystals was characterized by a combination of Rutherford backscattering spectrometry (RBS) and elastic recoil detection analysis (ERDA) with a 3 MeV ^{4}He beam and with Raman spectroscopy. Both RBS and ERDA are nondestructive methods based on high-energy ion scattering, providing depth-resolved information about the elemental composition of near-surface layers [17,18]. Depth profiles for Li were measured with RBS with the He ion beam incident normal to the sample surface and backscattered into a glancing-angle detector located at 103° from the incident beam direction. Analysis of RBS and ERDA spectra was done with the RUMP code [19].

The RBS spectrum from a representative crystal is shown in Fig. 3. Surface peaks of the elements detected are shown by arrows. A peak present at particular scattering energy indicates the presence of an element of a particular mass. Figure 3 shows that the bulk of the crystal is composed of ^{6}Li isotope, with an upper bound for the ^{7}Li/^{6}Li atomic fraction of 5 at.%. No counts were measured at scattering energies above 1.76 MeV, indicating that concentrations of impurities heavier than oxygen are negligible. Oxygen and carbon peaks do not extend to lower energies, which is consistent with the presence of a thin corrosion layer on the LiH crystal surface. The total C and O areal densities are $\sim 10^{16}$ and $\sim 10^{17}$ at/cm^2, respectively, corresponding to a ~30-nm-thick LiOH surface corrosion layer with negligible C. This surface layer is not

TABLE I. Initial pressure of samples precompressed in a diamond anvil cell, and the subsequent effect on the initial density and index of refraction of LiH and quartz.

Shot #	P (GPa)	LiH ρ_0 (g/cm^3)	LiH n	Quartz ρ_0 (g/cm^3)	Quartz n
66039	0.59(.03)	0.699(.003)	2.022(.007)	2.698(.003)	1.553(.003)
66034	0.72(.03)	0.702(.003)	2.026(.007)	2.689(.003)	1.554(.003)
66486	0.92(.03)	0.705(.003)	2.029(.007)	2.711(.003)	1.556(.003)

unexpected, given the high reactivity of LiH [14]. However, such a thin surface layer will have a negligible effect on our experimental results. The lack of any detectable O and C contamination in the crystal bulk gives confidence that our sample is a full-density single crystal, without porosity.

Depth profiles of H were measured with ERDA with the sample normal direction tilted to 70° with respect to the incident beam direction, and hydrogen atoms recoiled at 150° were measured with a surface barrier detector covered with a 10-μm-thick carbon foil. Results of the ERDA analysis indicate a negligible deuterium content in the LiH crystals, with H/D ratios <0.1%.

We use vibrational spectroscopy to further confirm the bulk purity and the H species. Li-D vibrational modes have significantly lower frequency than the corresponding Li-H vibrations [20]. A Raman spectroscopy measurement of a representative LiH sample is shown in Fig. 4. Vertical lines show the ideal second-order Raman peak positions for LiH and LiD (Li isotopic species has a very minor effect on the peak positions [21]) and clearly identify our bulk crystal as pure LiH. We also see no evidence for LiOH [22], Li_2O [23], LiOH*H_2O [24], or Li_2CO_3 [25], which are the reaction products known to form when LiH is exposed to moisture [20] and all of which have strong Raman features compared to the weak, second-order scattering from LiH. These two measurements confirm the bulk isotopic content and purity of the sample, identifying it as uncontaminated, nonporous single crystal ^{6}LiH with a maximum of 5 at% ^{7}Li. Taking into account the uncertainty in ^{7}Li content, we assume an initial density of 0.687(±0.003) g/cm^3.

The index of refraction of LiH and quartz have an effect on the measured *in situ* shock velocity ($D_{\text{actual}} = D_{\text{measured}}/n$). The index of LiH at the VISAR wavelength of 532 nm is

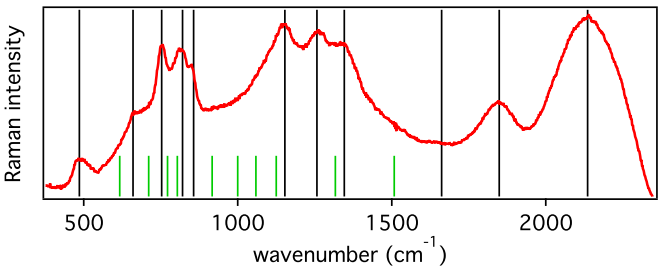

FIG. 4. Raman spectroscopic measurement of second-order modes in the LiH sample used for this study. The ideal peak positions shown in black are from ^{6}LiH, at 10 Kelvin (with the addition of one low-wave-number peak that appears at higher temperature). Ideal peak positions for ^{7}LiD are shown with the short green line (^{6}LiD peak positions are not known, but Li isotope species has a very minor effect on peak position [21]).

2.009(±0.005), from Ref. [26]. This value was tested for our crystal using the Brewster's angle method and found to be consistent to ~1%. The method used in the previous study, refraction by prisms cut from single crystals [27], was unsuitable for our targets but is intrinsically more accurate because it is less sensitive to surface hydrolysis, so we use the literature value. The index of quartz at the visar wavelength is 1.54687 [28] and its density dependence is derived from Ref. [29], as described in Appendix A of Ref. [30]. No studies have constrained the variation in LiH index as a function of increasing density. The variation is often expressed by the density derivative of the Lorentz-Lorenz relation, as shown in Ref. [29]: $\partial n/\partial\rho = [(n^2-1)(n^2+2)/6n\rho](1-\Lambda_0)$, requiring some constraint on the strain polarizability parameter Λ_0, which is also unknown in the LiH literature. An alternative method for calculating this trend based on changes in density and electronic band gap is described in Ref. [31]. The $n(\rho)$ relation is derived from on an approximation to the expression for the dielectric function which is appropriate in cases where the conduction band has a pronounced minimum as a function of wave vector; reasonable for the case of LiH [32]. The change in band gap as a function of pressure was measured previously [33], and below 1 GPa is increasing at a rate of approximately 0.5 meV/GPa. The index variation calculated with this latter approximation is consistent with the Lorentz-Lorenz trend with a value of 0.5 for the strain polarizability parameter Λ_0. The LiH indexes calculated for the three precompressed samples are shown in Table I. Uncertainty is based on the uncertainty in density and ambient refractive index. Systematic uncertainty in the approximation for $\partial n/\partial\rho$ is not included.

IV. EXPERIMENTAL DESIGN SIMULATIONS

We have used computer calculations with the HYDRA program [34] to aid in the design and interpretation of the shock EOS experiments. HYDRA simulates the propagation and absorption of the laser pulses, heating of the plasma, radiative and conductive energy transport, and hydrodynamics. Most simulations assume one-dimensional planar geometry, with a multiplier of 0.75 on the laser intensity, which has been determined by comparison to previously published shock velocity data for quartz/glow-discharge polymer (CH) targets [35]. Two-dimensional simulations indicate that the transverse laser intensity distribution and energy transport effects can account for this multiplier. The HYDRA simulations use equation-of-state tables to give the pressure and internal energy as functions of the temperature and density of the material. The tables have been generated with the QEOS model [36], including improvements that allow an EOS to be fitted to experimental Hugoniot, isothermal, and critical point data [37]. The LiH table was fitted to Hugoniot data at

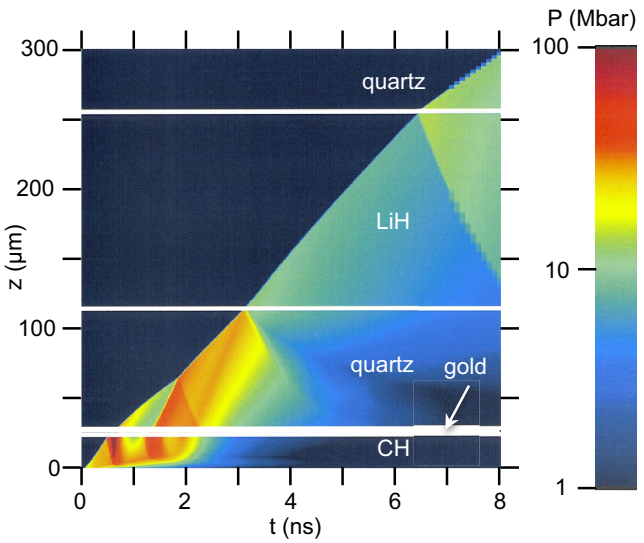

FIG. 5. HYDRA simulations of the pressure profile across a representative target as a function of position and time.

pressures below 50 GPa [38] and one data point at 1200 GPa [39]. The electronic properties of the CH and SiO2 (quartz) tables are based on the Thomas-Fermi statistical model. The electronic part of the LiH EOS has been calculated with a more accurate self-consistent-field ion-in-cell model [40], using the PURGATORIO code [41,42], which calculates the shell ionization structure.

The simulations produce time- and space-dependent values for physical properties of the target material, such as temperature, density, and pressure. The response of a typical target can be seen in Fig. 5, showing pressure versus time and position. Of particular importance is the wave reverberation that begins as the initial shock reflects from the CH/Au interface at 0.5 ns. When this reflected shock reaches the ablation front at 0.6 ns, the ensuing expansion causes a release wave to run back into the sample. The drive laser is on for another nanosecond so a second shock forms and catches up with the first shock in the middle of the quartz layer at 1.8 ns. We use simulations to design the target and drive to avoid the reverberation landing too near an interface, which results in an ambiguous measurement.

Simulations have also aided in understanding the degree of preheating of the LiH by x rays generated in the laser interaction region of the target, which will affect the initial density and move the measurement away from the principal Hugoniot. The targets fielded for this experiment contained 2- to 5-μm-thick gold layers between the CH and quartz to reduce the amount of radiation reaching the quartz and LiH layers. We find that, at the highest drive intensities for which analyzable data was obtained (s70347,I $= 4.4 \times 10^{14}$ W/cm^2), the effect of x rays is predicted to be extremely small, producing less than 10^{-4} eV (1K) temperature rise in the LiH.

V. RESULTS

The Hugoniot state in LiH was determined from the measurement of velocities of reflecting shock waves in quartz and LiH. At the interface between them, the pressure and particle velocity in the two materials must be equal (the impedance-matching constraint), so knowledge of the quartz Hugoniot and the release states corresponding to the measured shock velocity yields the pressure and particle velocity in LiH. The most recent quartz standard (Hugoniot and release model) [30] was used for all results presented in this paper. See Supplemental Material [43] for an analysis using an alternate recent quartz model [44]. The Hugoniot jump conditions are then used to calculate all other shock front variables. We report experimental observables in Table II. It is important to note that the quartz Hugoniot has been experimentally constrained only up to shock velocities of 33 km/s, and the isentropic releases measured from shock states up to 25 km/s. The highest-pressure measurements reported here are beyond this range and thus require an extrapolation of the existing quartz standard (using the functional form from Ref. [30]). The analyzed data will need to be confirmed in the future when the quartz standard is extended.

TABLE II. Experimental data: Drive intensity, initial LiH density (ρ_0); quartz and LiH shock velocities at the interface (D); LiH particle velocity (U); pressure (P); density (ρ); compression (η); and temperature (T). Missing temperature measurements were from shots taken on the Omega-EP laser facility, where the streaked optical pyrometer diagnostic was not available. The numbers in brackets correspond to one standard deviation.

Shot #	Drive intensity (W/cm^2)	LiH ρ_0 (g/cm^3)	Quartz D (km/s)	LiH D (km/s)	LiH U (km/s)	LiH P (GPa)	LiH ρ (g/cm^3)	LiH η	LiH T (eV)
66 039[a]	4.14e14	0.699(.003)	19.2(.3)	24.3(.2)	15.1(.4)	257(6)	1.85(.08)	2.65(.11)	1.06(.05)
16 252	4.83e13	0.687(.003)	19.7(.3)	24.6(.3)	15.8(.4)	267(8)	1.90(.11)	2.77(.15)	
66034[a]	4.91e14	0.702(.003)	20.9(.1)	26.1(.2)	16.9(.1)	310(3)	1.98(.04)	2.82(.06)	1.33(.03)
16 251	4.81e13	0.687(.003)	21.7(.3)	27.6(.3)	17.7(.4)	336(8)	1.93(.10)	2.81(.14)	
66 486[a]	3.18e14	0.705(.003)	22.9(.4)	28.5(.4)	19.0(.5)	384(10)	2.12(.12)	3.00(.18)	1.72(.04)
69 550	2.32e14	0.687(.003)	27.5(.3)	35.6(.3)	24.0(.5)	587(12)	2.12(.09)	3.08(.14)	3.07(.08)
72 663	2.69e14	0.687(.003)	29.6(.3)	37.7(.3)	26.4(.5)	683(14)	2.29(.11)	3.33(.17)	3.34(.10)
70 346	3.73e14	0.687(.003)	33.2(.3)	42.7(.3)	30.2(.5)	885(17)	2.35(.11)	3.42(.16)	5.00(.11)
70 336	3.52e14	0.687(.003)	35.2(.4)	45.1(.5)	32.4(.6)	1005(22)	2.44(.15)	3.55(.21)	5.81(.18)
70 347	4.42e14	0.687(.003)	36.6(.5)	47.3(.5)	33.8(.8)	1100(27)	2.41(.16)	3.51(.23)	6.59(.28)

[a]Diamond anvil cell samples.

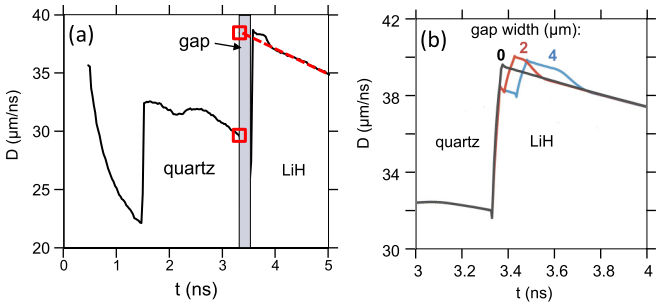

FIG. 6. (a) Velocities at the quartz-LiH interface with a micron-scale gap of mineral oil between the surfaces for shot 72 663. HYDRA simulations shown in (b) illustrate expected behavior for three different gap widths. The extrapolation method used to determine velocities for the impedance-matching analysis is shown in (a) and the uncertainties associated with this extrapolation are illustrated with the red boxes.

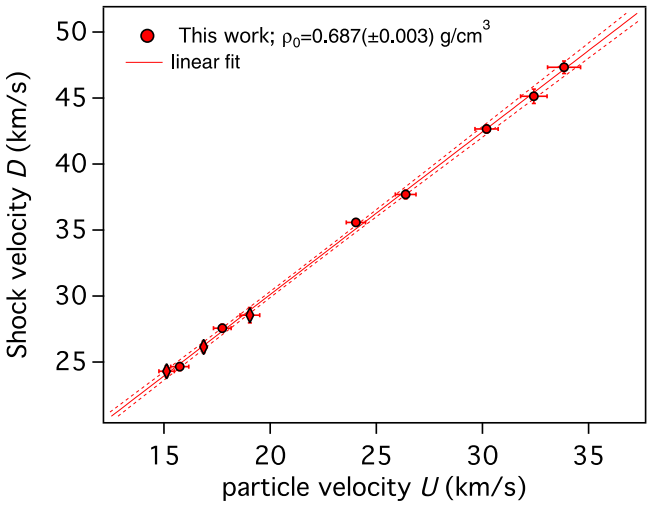

FIG. 7. Experimental data with linear fit to $D(U)$ and 68% confidence bands. Data points from the precompressed measurements are represented by diamond-shaped symbols.

In the cases where layers of mineral oil were present at the impedance-matching interfaces, wave interactions within the thin layer perturb the velocities at the interface. HYDRA simulations (Fig. 6) indicated that the late-time velocity trend is not affected by these perturbations and so we extrapolated back the later-time smooth velocity trend in the LiH through the mineral oil to the rear surface of the quartz and performed the impedance matching at the time of the quartz breakout. The uncertainty in this extrapolation contributed to the uncertainties in LiH shock velocities reported in Table II. Other sources of experimental uncertainty include an inherent uncertainty of ±3% of a VISAR fringe shift in the LiH and quartz velocities, and systematic uncertainties in the initial density and index of refraction of the quartz and LiH, and in the quartz reference equation of state.

Stationary optical interfaces between materials in the target with differing index of refraction (LiH-mineral oil, mineral oil-quartz) reflect a percentage of the VISAR light back into the interferometer, appearing as a set of unshifted ghost fringes superposed over the Doppler-shifted fringes from the moving shock front. The fringing data is analyzed by expressing it as a complex wave, and the ghost fringe removed by subtracting a complex constant that centers the data when plotted as a Lissajous curve. The quality of centration is diagnosed by plotting the absolute value of the complex fringing wave as a function of the nonfringing intensity and optimizing the linearity (details given in Ref. [45]).

The measured shock velocity as a function of analyzed particle velocity (Fig. 7) follows an apparently linear trend over this range. We fit the data with a linear function: $D = a + b(U - c)$, with c fixed at a value chosen to best diagonalize the covariance matrix. The best fit yielded $a = 31.351 \pm 0.226$, $b = 1.232 \pm 0.038$, and $c = 21.01$.

The temperature (T) is determined from a comparison of the intensity (I) of optical emission from the shock front in LiH and in quartz, and can be expressed using the relation: $T = T_0/ln[1 + (1 - R)A/I]$, where T_0 is the spectral response of the system, which was independently determined to be 1.91 eV for these measurements, and A is a calibration constant that varies somewhat depending on VISAR telescope alignment from shot to shot. R is the reflectivity of 532-nm VISAR laser light and $(1 - R)$ is the gray-body approximation for the emissivity. For quartz, the temperature and reflectivity as a function of shock velocity have been previously calibrated and thus can be used as absolute references for the measurement in LiH. The quartz temperature for shock velocities between 10 and 24 km/s was taken from Ref. [46], and above 25 km/s from Ref. [47]. The reflectivity reference is taken from shocked silica measurements [46] with functional form given in Ref. [47]. Since the shock velocity in quartz is measured using VISAR, quartz temperature is known and can be correlated with the measured SOP counts. Reflectivity is also known and can be correlated with measured intensity of the reflected VISAR light. The relation can therefore be inverted to find A, which is then used in the same relation to determine the LiH temperature, given the measured SOP counts and VISAR reflectivity from the reflecting shock in LiH. The presence of ghost fringes, which in some cases have an intensity up to nearly 60% of the Doppler-shift fringe intensity, will have an effect on the inferred reflectivity. The "vector offset" method [45] effectively separates and removes the unshifted intensity. Additionally, since the LiH reflectivity is low, the expression for temperature is not dominated by the $(1 - R)$ term, and variations of up to 10% in the reflectivity will have a $< 2\%$ effect on the inferred temperature.

The SOP counts give a continuous time history of the thermal emission as the shock wave propagates through the LiH sample. For a decaying shock wave, this will yield a continuous record of temperature as a function of shock velocity along the principal Hugoniot. In this case, however, some absorption of visible light in unshocked LiH between the shock front and the spectrometer results in an additional time-varying change in reflectivity and emission over the SOP sweep window. Optical absorption is known to occur in radiation-induced color-centers in LiH [48], and the energy and width of the LiH impurity bands vary based on wavelength and duration of irradiation (sources as weak as ordinary daylight cause some F-center formation) and on sample temperature and thermal history. These effects were not controlled in the

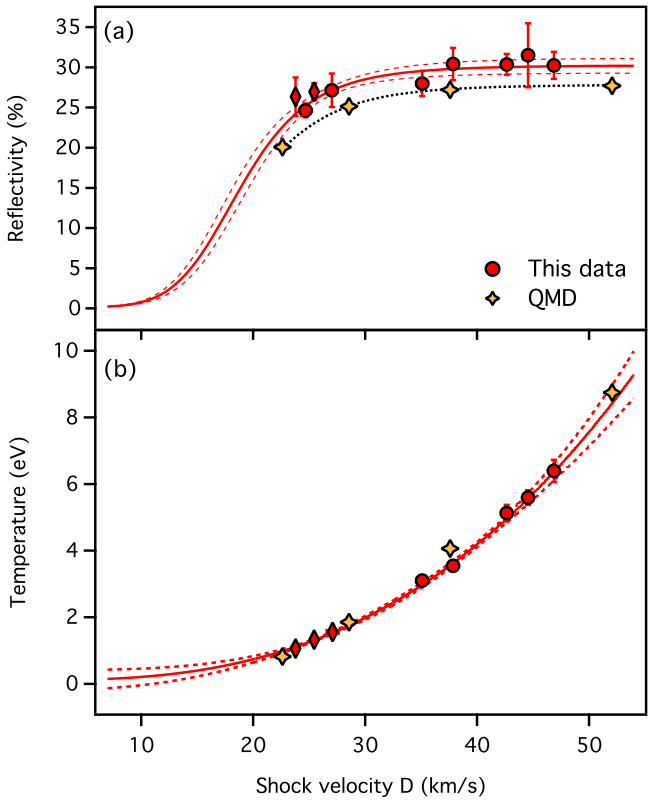

FIG. 8. (a) LiH reflectivity from the shocked/unshocked LiH interface at 532 nm as a function of shock velocity, fit with the function described in the text, compared to first principles predictions. (b) Temperature as a function of shock velocity fit with a power law: $T = 0.12(\pm 0.31) + 0.00019(\pm 0.00029) * U_s^{2.70(\pm 0.38)}$. Dashed lines are 68% confidence bands. Data points from precompressed samples are represented by diamond-shaped symbols.

experiment so, to avoid approximations, we determine the reflectivity and temperature in LiH only immediately after the wave propagates across the quartz-LiH interface.

As shown in Fig. 8(a), the reflectivity from the interface between shocked and unshocked LiH as a function of shock velocity appears to increase slightly initially and then reaches a value of 30%, indicating that ionization has already occurred at the lowest pressure we measure, and it undergoes little further change up to the highest pressure. Since our data is relatively flat and scattered, we use quantum molecular dynamics (QMD) simulations to help establish a reasonable trend. QMD calculations were performed with the Quantum Espresso package [49]. The local density approximation to the exchange-correlation functional was employed in all DFT calculations. To keep plane-wave cutoffs within a reasonable value, we used norm-conserving Troullier-Martins pseudopotentials [50] to describe both hydrogen and lithium, with core radii of 0.2 a.u. and 0.45 a.u., respectively. All electrons were included in the valence space. The simulation cell contained 64 atoms and calculations were performed at the Γ point using a plane-wave cutoff of 300 Ry. Thermodynamic properties were corrected for the finite plane-wave cutoff and simulation cell used in the simulations. To do this, we calculated a density- and temperature-dependent correction to the pressure and internal energy obtained by post-processing several dozen configurations at each state point with a plane-wave cutoff of 1000 Ry and a $3 \times 3 \times 3$ k-point grid, both of which were found to be enough to fully converge these quantities. Optical properties were calculated using the Kubo-Greenwood formulation [51], by performing excited state calculations on ∼16 statistically independent ionic configurations at every temperature and density. The onset of metal-like reflectivity, followed by the presence of a plateau over the shock velocity range of our experiments, is consistent with our measurements.

To calculate the temperature we use a Hill equation fit to the reflectivity as a function of shock velocity [Fig. 8(a), with 1σ confidence bands shown], with base and rate fixed by the QMD trend in this range:

$$R(D)_{532} = 0.164 + \frac{30.27(\pm 0.93) - 0.164}{1 + ((19.09(\pm 0.86)/D)^{6.075}}. \quad (1)$$

The uncertainty in this fit results in less than 1% uncertainty in the calculated temperature, shown in Fig. 8(b). The noise in the pyrometer signal contributes 1–5% random uncertainty.

This experimentally determined pressure and temperature along the principal Hugoniot are plotted in Fig. 9 as functions

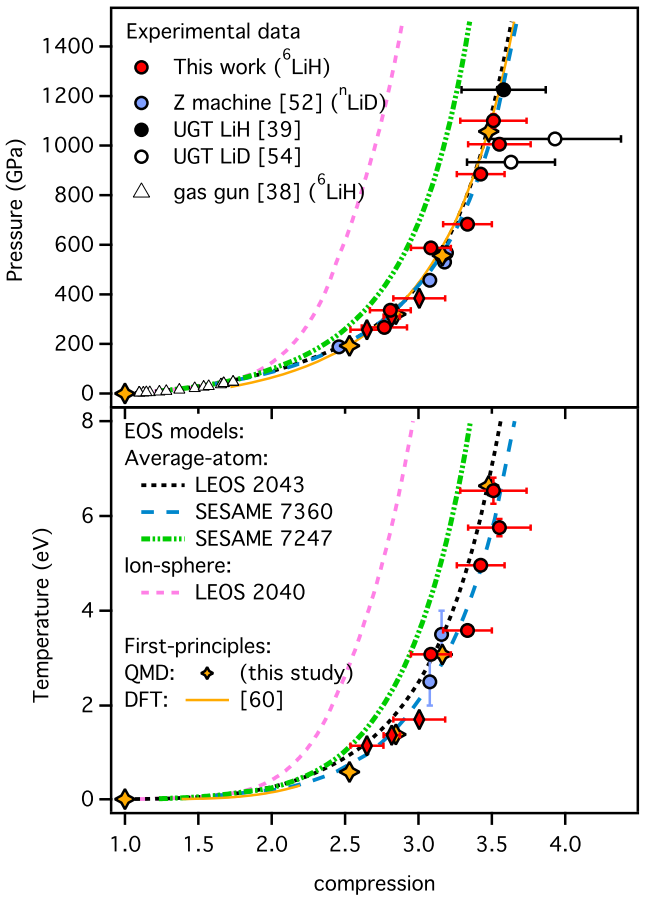

FIG. 9. Experimental results compared to previous measurements from the Z machine [52], from gas guns [38], and from underground tests [39,54]; theoretical predictions from QMD (this work, in close agreement with Refs. [52,53,59] and density functional theory [60]; and tabulated equation of state models [59,61]. Precompressed data points are shown as diamond-shaped red symbols.

TABLE III. Reanalyzed UGT Hugoniot data from LiD

Standard	U (km/s)	P (GPa)	η
Mo	29.2(.7)	933(35)	3.63(.3)
Be	31(1)	1027(16)	3.93(.45)

of compression, to allow direct comparison to measurements performed on other LiH isotopes with different initial densities [38,39,52,54].

There is a subtle difference between the sample locations where the pressure and the temperature measurement are made. The pressure is determined from the shock velocity immediately after the breakout from quartz, requiring an extrapolation of the velocity histories across a sizable mineral-oil gap in some cases. The temperature, however, is measured in the LiH just after the shock wave has entered it, with no extrapolation. Therefore, to plot the temperatures corresponding to the experimentally determined compression states, we fit the temperature data with a power law [Fig. 8(b)], and the temperature and uncertainties corresponding to the experimental compression states are from that model fit.

The high-pressure underground test (UGT) data shown in Fig. 9 from Refs. [39,54] were collected on LiD and LiH samples. The LiD measurements were made using Mo and Be as impedance-matching standards and using the SESAME equation of state tables 2981 and 2020 for Mo and Be, respectively. We have reanalyzed these results using more recent equations of state for the standard materials: tabulated EOS (Mo-LEOS-420 and Be-LEOS-40), which better fit experimental data not available at the time these measurements were performed (i.e., Refs. [55,56]). We obtain new values of U, P, and $\eta = \rho_0/\rho$ reported in Table III. In the LiH experiment [39], the authors used a carbon standard and the SESAME 7831 to interpret the data. This table fits well recent data on C from Refs. [57,58], so we show the original result in Fig. 9.

There is excellent agreement between the results from this work and the Z machine study (and, within the error bars, with the underground test measurements), indicating that the differing time scales do not cause a systematic discrepancy in the results.

Several different model predictions for the principal Hugoniot are also compared to the experimental data in Fig. 9. The EOS models are based on a three-component free energy consisting of a zero-temperature cold curve, an ion-thermal component (describing the zero point and thermal motion of the ions), and an electron-thermal component (describing the thermal excitation of electrons from the ground state). The models shown differ primarily in their treatment of the electron-thermal component and are grouped accordingly. LEOS 2043 uses an average-atom DFT (Purgatorio [42]) description of the electron-thermal component, and is fit to a wide-ranging set of ab inito data from QMD (a subset of which is shown here) and path integral Monte Carlo simulations (details will be part of a future publication), and experimental data sets, including this data, the data from the Z-machine [52], and lower pressure measurements, including porous

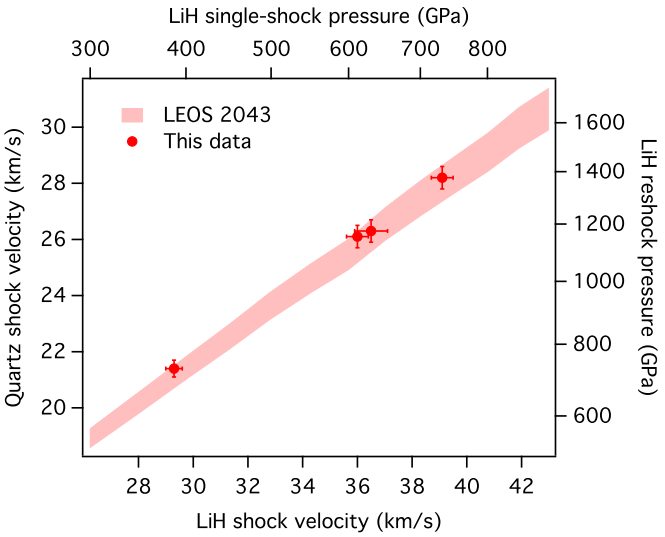

FIG. 10. Measured shock velocities at the second LiH-quartz interface, compared to the LEOS 2043 model prediction. The LEOS table has been scaled in density to describe the ^{6}LiH isotope. The line width represents uncertainty in the experimental quartz Hugoniot.

Hugoniots [38] and isotherms [13]. The SESAME models use a Thomas-Fermi-Dirac average-atom model for the electron-thermal component. SESAME 7360 is built on a combination of experimental data at low pressure and ab initio molecular dynamics simulations of the Hugoniot in the pressure regime of this study, as described in Ref. [59]. The two recent LEOS and SESAME models yield nearly identical results for the pressure-density Hugoniot (not surprisingly, since they are fit to very similar ab initio data). SESAME 7247 uses essentially the same models for the cold curve and electron-thermal components as SESAME 7360, but for SESAME 7360 the ion-thermal component was corrected to include a density-dependence to the thermodynamic Grüneisen parameter γ [62] (the LEOS models also contain a density-dependent Grüneisen term). The older LEOS 2040 model uses an ion-sphere (Thomas-Fermi) approximation to the electron thermal component, which excludes all atomic shell-structure effects.

The experimental measurements provide clear evidence for the validity of the average-atom-based equation of state models for LiH, compared to the ion-sphere model, over this range, and suggest that the Grüneisen parameter has a density dependence.

For a subset of the shots, the decaying shock wave in the LiH hit a second quartz window, resulting in a shock in the quartz and a reshock back into the lower-impedance LiH. We can use this data to put additional constraints on EOS models, in an off-Hugoniot regime where experimental data are even sparser. In Fig. 10, we compare the experimental shock velocities with those predicted by LEOS 2043 (scaled to the ^{6}LiH isotope), generated by impedance matching the series of LEOS 2043 second-shock states with the experimental quartz Hugoniot. Within the uncertainty (which is really the uncertainty in the experimental quartz Hugoniot extrapolation), the model accurately describes these off-Hugoniot states as well.

TABLE IV. Double-shock data: measured shock velocities at the second LiH-quartz interface (LiH D_1 and Quartz D) and second-shock Hugoniot state (LiH P_2, ρ_2) from impedance-matching with quartz. LiH γ calculated based on comparison to a reference state on the cold curve.

Shot #	LiH D_1 (km/s)	Quartz D (km/s)	LiH P_1	LiH ρ_1 (g/cm^3)	LiH P_2 (GPa)	LiH ρ_2 (g/cm^3)	LiH γ
72663	29.3(.3)	21.4(.3)	389(10)	2.02(.04)	730(24)	2.69(.24)	0.73(.25)
70346	36.0(.4)	26.1(.4)	613(16)	2.21(.05)	1155(40)	3.00(.30)	0.71(.21)
70336	36.5(.6)	26.3(.4)	632(24)	2.22(.05)	1175(41)	3.09(.41)	0.65(.24)
70347	39.1(.4)	28.2(.4)	733(15)	2.28(.05)	1376(44)	3.16(.31)	0.67(.18)

The LiH single-shocked state at the interface (P_1, U_1, ρ_1), which is decayed after traversing the LiH sample, can be calculated from the measured shock velocity (D_1) and the experimental equation of state (Fig. 7). The pressure (P_2) and particle velocity (U_2) of the reshock state are known from impedance-matching with the quartz window, and thus determined from the measurement of the quartz shock velocity and the known quartz equation of state. The remaining EOS parameters for the reshocked LiH (ρ_2, D_2) are determined from the mass and momentum Hugoniot jump conditions:

$$\rho_2(D_2 - U_2) = \rho_1(D_2 - U_1), \tag{2}$$

$$P_2 - P_1 = \rho_1(D_2 - U_1)(U_2 - U_1). \tag{3}$$

Results are reported in Table IV. Measurements on the Z machine also probed the set of second-shock Hugoniot states impedance-matched to quartz and are in good agreement.

One can calculate a Grüneisen parameter (assumed to depend on density only) relative to a reference state (E_R, P_R) on an isentropic equation of state, using the Hugoniot jump condition for the first and second shocks:

$$E_1 - E_0 = \frac{1}{2}(P_1 + P_0)\left(\frac{1}{\rho_0} - \frac{1}{\rho_1}\right), \tag{4}$$

$$E_2 - E_1 = \frac{1}{2}(P_2 + P_1)\left(\frac{1}{\rho_1} - \frac{1}{\rho_2}\right), \tag{5}$$

and a Mie-Grüneisen equation of state:

$$E_2 - E_R = \frac{V}{\gamma}(P_2 - P_R). \tag{6}$$

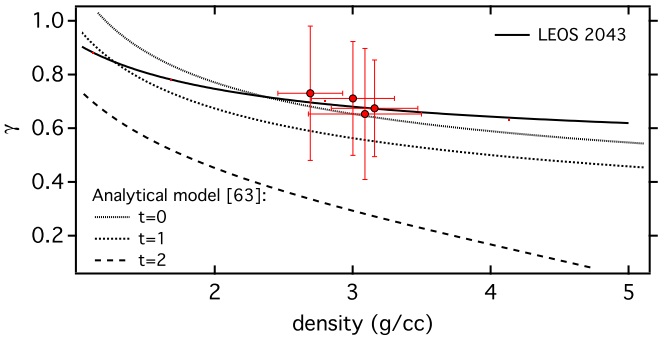

FIG. 11. Grüneisen parameter calculated from the energy difference between second-shock states and states at a corresponding density on the 300 K isotherm. The data is compared to model LEOS 2043 (isotopically scaled), and to several analytical models ($t = 0$ [64], $t = 1$ [65], $t = 3$ [66], described in the text).

We approximate the isentrope by the room temperature isotherm, extrapolated to high densities using the Vinet equation of state:

$$E_R - E_0 = \frac{2B_0}{\rho_0 K^2}\left\{2 - [5 + 3(XK - B_0')]e^{(-\frac{3}{2}K(X-1))}\right\}, \tag{7}$$

with $K = (B_0' - 1)$ and $X = (\rho_0/\rho_2)^{1/3}$. B_0 and B_0', the bulk modulus and pressure derivative of the bulk modulus, were taken from Ref. [13] (extrapolated above 3.1-fold compression, which is the limit of the experimental data). The derived second-shock states and Grüneisen parameter are shown in Table IV and Fig. 11. A Monte Carlo method is used to propagate the uncertainties in shock velocity measurement and in the quartz and LiH single-shock EOS fitting parameters to the final pressure, density, and Grüneisen parameter associated with the second shock state. The Grüneisen parameter is compared with an analytical model for the density dependence, formulated in Ref. [63]:

$$\gamma = \frac{B'/2 - 1/6 - t/3(1 - P/3B)}{1 - 2tP/3B}, \tag{8}$$

where P is the pressure on the cold curve (approximated by the 300 K isotherm, previously measured up to a compression of 3.1 [13]). $B = -VdP/dV$ and $B' = (dB/dV)/(dP/dV)$ are also calculated based on the Vinet equation of state from Ref. [13]. The value for t is suggested to be an increasing function of density [63]. Our data are too sparse to constrain the density dependence of t, but over the range of the double-shocked data, they are most consistent with the case of $t = 0$, the Slater form [64]. The Grüneisen parameter used for LEOS 2043, which is an adjustable parameter in the formulation, is also in good agreement with the experimental data. The choice of Grüneisen parameter and its density dependence can have a significant effect on the EOS, as shown in Refs. [59,67]. The more recent SESAME EOS tables for LiD were formulated with the assumption that $\gamma_0 \sim 1$, and decreases slowly toward a limiting value of 2/3 as $\rho \to \infty$ [67]. This data confirms the validity of a density-dependent Grüneisen parameter and suggests that the limit is lower than 2/3, consistent with multiple theoretical predictions for the limiting state of a solid as 1/2 [[59], and references therein].

VI. CONCLUSIONS

Measurements of the pressure, density, temperature, and single-wavelength reflectivity along the principal Hugoniot have been extended to 1100 GPa and on a second-shock Hugoniot state up to 1376 GPa and near fivefold compression. Reflectivity measurements are consistent with earlier findings

[68] that Li has partially ionized by 2.5-fold compression, and the lack of further increase in reflectivity up to 3.5-fold compression indicates that the inner Li and H electronic shells remain intact. The *ab initio* data are in good agreement with experimental results and thus the average-atom Purgatorio and SESAME EOS models, which are fit to those data, are found to accurately describe the shock compressibility over this regime, while the Thomas-Fermi model is found to be too stiff. Double-shock data give additional confidence in the average atom models. The Grüneisen parameter, calculated using a Mie-Grüneisen formalism and based on experimental measurements of the cold curve (extrapolated to higher pressures) and the second-shock Hugoniot measurements, suggest a density-dependent Grüneisen parameter in the Slater form.

ACKNOWLEDGMENTS

We acknowledge T. Uphaus for help with target fabrication, Zs. Jenei for help with Raman spectroscopy measurements, and N. Whiting and C. Sorce for experimental support at the Laboratory for Laser Energetics. This work was performed under the auspices of the U.S. Department of Energy by Lawrence Livermore National Laboratory under Contract No. DE-AC52-07NA27344. Lawrence Livermore National Security, LLC.

[1] L. George and S. K. Saxena, Int. J. Hydrogen Energy **35**, 5454 (2010).
[2] E. L. P. y Blanca and R. del P. N. Maldonado, Eur. Phys. J. B **87**, 110 (2014).
[3] P. Loubeyre, R. Le Toullec, M. Hanfland, L. Ulivi, F. Datchi, and D. Hausermann, Phys. Rev. B **57**, 10403 (1998).
[4] D. Mukherjee, B. D. Sahoo, K. D. Joshi, Satish C. Gupta, and S. K. Sikka, J. Appl. Phys. **109**, 103515 (2011).
[5] L. X. Benedict, K. P. Driver, S. Hamel, B. Militzer, T. Qi, A. A. Correa, A. Saul, and E. Schwegler, Phys. Rev. B **89**, 224109 (2014).
[6] L. Caillabet, S. Mazevet, and P. Loubeyre, Phys. Rev. B **83**, 094101 (2011).
[7] S. X. Hu, B. Militzer, L. A. Collins, K. P. Driver, and J. D. Kress, Phys. Rev. B **94**, 094109 (2016).
[8] S. Hamel, L. X. Benedict, P. M. Celliers *et al.*, Phys. Rev. B **86**, 094113 (2012).
[9] C. W. Cranfill and R. More, Los Alamos Scientific Laboratory Report LA 7313-MS, 1978.
[10] L. Merrill and W. A. Bassett, Rev. Sci. Instrum. **45**, 290 (1974).
[11] A. Dewaele, P. Loubeyre, and M. Mezouar, Phys. Rev. B **70**, 094112 (2004).
[12] E. Calderon, M. Gaulthier, F. Decremps, G. Hamel, G. Syfosse, and A. Polian, J. Phys.: Condens. Matter **19**, 436228 (2007).
[13] A. Lazicki, P. Loubeyre, F. Occelli, R. J. Hemley, and M. Mezouar, Phys. Rev. B **85**, 054103 (2012).
[14] L. M. Barker and R. E. Hollenbach, J. Appl. Phys. **43**, 4669 (1972).
[15] P. M. Celliers, D. K. Bradley, G. W. Collins, D. G. Hicks, T. R. Boehly, and W. J. Armstrong, Rev. Sci. Instrum. **75**, 4916 (2004).
[16] J. E. Miller, T. R. Boehly, A. Melchior, D. D. Meyerhofer, P. M. Celliers, J. H. Eggert, D. G. Hicks, C. M. Sorce, J. A. Oerte, and P. M. Emmel, Rev. Sci. Instrum. **78**, 034903 (2007).
[17] W.-K. Chu, J. W. Mayer, and M. A. Nicolet, *Backscattering Spectrometry* (Academic Press, New York, 1978)
[18] J. Tirira, Y. Serruys, and P. Trocellier, *Forward Recoil Spectrometry* (Plenum Press, New York, 1996).
[19] L. R. Doolittle, Nucl. Instrum. Methods Phys. Res., Sect. B **9**, 344 (1985).
[20] C. L. Haertling, R. J. Hanrahan, Jr., and J. R. Tesmer, J. Phys. Chem. C **111**, 1716 (2007).
[21] A. Anderson and F. Luty, Phys. Rev. B **28**, 3415 (1983).
[22] Y. Hase and I. V. Pagotto Yoshida, Chem. Phys. Lett. **65**, 46 (1979).
[23] T. Osaka and I. Shindo, Solid State Commun. **51**, 421 (1984).
[24] V. I. Tyutyunnik, J. Raman Spectrosc. **31**, 559 (2000).
[25] M. H. Brooker and J. B. Bates, J. Chem. Phys. **54**, 4788 (1971).
[26] E. Staritzky and D. I. Walker, Anal. Chem. **28**, 1055 (1956).
[27] C. E. Messer, "A Survey Report on Lithium Hydride", NYO-9470, Oct. 27, 1960.
[28] G. Ghosh, Opt. Commun. **163**, 95 (1999).
[29] K. Vedam and T. A. Davis, J. Opt. Soc. Am. **57**, 1140 (1967).
[30] S. Brygoo, M. Millot, P. Loubeyre, A. E. Lazicki, S. Hamel, T. Qi, P. M. Celliers, F. Coppari, J. H. Eggert, D. E. Fratanduono, D. G. Hicks, J. R. Rygg, R. F. Smith, D. C. Swift, G. W. Collins, and R. Jeanloz, J. App. Phys. **118**, 195901 (2015).
[31] M. S. T. Bukowinski, J. Geophys. Res. **85**, 285 (1980).
[32] S. Lebegue, M. Alouani, B. Arnaud, and W. E. Pickett, Europhys. Lett. **63**, 562 (2003).
[33] Y. Kondo and K. Asaumi, J. Phys. Soc. Jpn. **57**, 367 (1988).
[34] M. M. Marinak, G. D. Kerbel, N. A. Gentile, O. Jones, D. Munro, S. Pollaine, T. R. Dittrich, and S. W. Haan, Phys. Plasmas **8**, 2275 (2001).
[35] M. A. Barrios, T. R. Boehly, D. G. Hicks, D. E. Fratanduono, J. H. Eggert, G. W. Collins, and D. D. Meyerhofer, J. Appl. Phys. **111**, 093515 (2012).
[36] R. M. More, K. H. Warren, D. A. Young, and G. B. Zimmerman, Phys. Fluids **31**, 3059 (1988)
[37] D. A. Young and E. Corey, J. Appl. Phys., **78**, 3748 (1995).
[38] S. P. Marsh, *LASL Shock Huginiot Data* (University of California Press, Berkeley, CA, 1980).
[39] C. E. Ragan, Phys. Rev. A **29**, 1391 (1984).
[40] D. A. Liberman, Phys. Rev. B **20**, 4981 (1979).
[41] B. Wilson, V. Sonnad, P. Sterne, and W. Isaacs, J. Quant. Spectrosc. Radiat. Transfer **99**, 658 (2006).
[42] P. A. Sterne, S. B. Hansen, B. G. Wilson, and W. A. Isaacs, High Energy Density Phys. **3**, 278 (2007).
[43] See Supplemental Material at http://link.aps.org/supplemental/10.1103/PhysRevB.96.134101 for an analysis using an alternate recent quartz model.
[44] M. D. Knudson and M. P. Desjarlais, Phys. Rev. B **88**, 184107 (2013).
[45] D. J. Erskine, J. H. Eggert, P. M. Celliers, and D. G. Hicks, Rev. Sci. Instrum. **87**, 033106 (2016).

[46] D. G. Hicks, T. R. Boehly, J. H. Eggert, J. E. Miller, P. M. Celliers, and G. W. Collins, Phys. Rev. Lett. **97**, 025502 (2006).
[47] M. Millot, N. Dubrovinskaia, A. Černok, S. Blaha, L. Dubrovinsky, D. G. Braun, P. M. Celliers, G. W. Collins, J. H. Eggert, and R. Jeanloz, Science **347**, 418 (2015).
[48] F. E. Pretzel and C. C. Rushing, J. Phys. Chem. Solids **17**, 232 (1961).
[49] P. Giannozzi *et al.*, J. Phys.: Condens. Matter **21**, 395502 (2009); http://www.quantum-espresso.org
[50] N. Troullier and J. L. Martins, Phys. Rev. B **43**, 1993 (1991).
[51] R. Kubo, J. Phys. Soc. Jpn. **12**, 570 (1957).
[52] M. D. Knudson, M. P. Desjarlais, and R. W. Lemke, J. Appl. Phys. **120**, 235902 (2016).
[53] D. V. Minakov and P. R. Levashov, Comput. Mater. Sci. **114**, 128 (2016).
[54] C. E. Ragan, Phys. Rev. A **25**, 3360 (1982).
[55] R. S. Hixon and J. N. Fritz, J. Appl. Phys. **71**, 1721 (1992)
[56] W. J. Nellis, J. A. Moriarty, A. C. Mitchell, and N. C. Holmes, J. Appl. Phys. **82**, 2225 (1997)
[57] M. D. Knudson, M. P. Desjarlais, and D. H. Dolan, Science **322**, 1822 (2008)
[58] D. G. Hicks, T. R. Boehly, P. M. Celliers, D. K. Bradley, J. H. Eggert, R. S. McWilliams, R. Jeanloz, and G. W. Collins, Phys. Rev. B **78**, 174102 (2008).
[59] D. Sheppard, J. D. Kress, S. Crockett, L. A. Collins, and M. P. Desjarlais, Phys. Rev. E **90**, 063314 (2014).
[60] Y. Wang, R. Ahuja, and B. Johansson, Phys. Status Solidi B **235**, 470 (2003).
[61] S. Crockett, SESAME 7246, in Los Alamos National Laboratory Report No. LA-UR-06-8403.
[62] J. Kress, L. A. Collins, L. Burakovsky, S. D. Herring, C. Ticknor, and S. Crockett, Los Alamos National Laboratory Report No. LA-UR-12-24783.
[63] L. Burakovsky and D. L. Preston, J. Phys. Chem. Solids **65**, 1581 (2004).
[64] J. C. Slater, *Introduction to Chemical Physics* (McGraw-Hill, New York, 1939), Chap. XII.
[65] J. S. Dugdale and K. C. MacDonald, Phys. Rev. **89**, 832 (1953).
[66] V. Y. Vashchenko and V. N. Zubarev, Fix. Tv. Tala, **5**, 886 (1963); Sov. Phys. Solid State **5**, 653 (1963).
[67] D. Sheppard, J. D. Kress, S. Crockett, L. A. Collins, and C. Greeff, Los Alamos National Laboratory Report LA-UR-15-27354.
[68] A. L. Kritcher, P. Neumayer, J. Castor, T. Doppner, R. W. Falcone, O. L. Landen, H. J. Lee, R. W. Lee, E. C. Morse, A. Ng, S. Pollaine, D. Price, and S. H. Genzer, Science **322**, 69 (2008).